Optimal design of nanomagnets for on-chip field gradients

W. Legrand,[1,*,†] S. Lopes,[1,2,†] Q. Schaeverbeke,[1] F. Montaigne,[2] and M.M. Desjardins[1]

[1] *C12 Quantum Electronics, Paris, France*

[2] *Université de Lorraine, Institut Jean Lamour, UMR CNRS 7198, Nancy 54011, France*

(Received 24 December 2022; revised 15 July 2023; accepted 21 July 2023; published 24 October 2023)

The generation of localized magnetic field gradients by on-chip nanomagnets is useful for a variety of technological applications, in particular, for spin qubits. To advance beyond the empirical design of these nanomagnets, we propose a systematic and general approach based on the micromagnetic formulation of an optimal field gradient source. We study the different field configurations that can be realized and find out quantitatively the most suitable ferromagnetic layer geometries. Using micromagnetic simulations, we then investigate the minimum requirements for reaching magnetic saturation in these nanomagnets. In terms of either longitudinal- or transverse-field gradient, the results provide an optimal solution for uniform, saturated nanomagnets, where the magnetic material can be selected according to the strength of the external fields that can be used.

DOI: 10.1103/PhysRevApplied.20.044062

I. INTRODUCTION

On-chip lithographed nanomagnets find a demanding application in the thriving field of quantum technologies, where they are used to generate locally magnetic field gradients. By shaping the energy spectrum of the electrons trapped in quantum dots, they allow for addressing spin qubits by microwave radiation, through the process of electric dipole spin resonance (EDSR) [1–3]. A strong and localized field gradient directly determines the coupling rate of a spin qubit to the microwaves, and is thus a key ingredient in several types of device operations [4–6]. Since the first successes of EDSR with nanomagnets, their design has been optimized through iterative improvements to increase the field gradients [7–11]. This enabled high-fidelity (99.9%) one-qubit gates on spin qubits with EDSR [12], reaching the threshold enabling successful error-correction codes. A next step is to enable high-fidelity two-qubit gates in devices hybridizing spins with single photons from on-chip microwave resonators [6,11,13], which requires even stronger field gradients. However, obtaining a strong inhomogeneity for the divergence-free, stray magnetic fields of the nanomagnets remains experimentally challenging, considering the length scale of around 100 nm that is relevant to these devices.

Most of the previous efforts have consisted in finding a suitable shape (commonly a split pair of aligned and elongated bars) for the patterned magnets to be placed in the vicinity of the quantum dot electrodes, in combination with increasing their thickness as much as possible. This has enabled significantly inhomogeneous magnetic field profiles at the nanoscale, with values of the field gradient approaching the order of 1 mT nm^{-1}. Between quantum dots typically separated by 60–120 nm, these gradients translate into a difference of about 30 mT [14] or 40 mT [11] for one of the field components, thereby modifying the local spin projection axis.

One might still wonder whether this approach is optimal in comparison to any possible geometry in general. Other shapes than a split pair of bar magnets have indeed been proposed and used in several contexts [15–18]. Optimal designs for these magnetic elements remain to be identified, even more when the nonuniformity of the internal magnetization is taken into account. We describe in this paper the realization of nanomagnets as close as possible from ideal magnetic field gradient sources, and identify several design rules relevant for practical nanolithographed devices on chip. Even though we discuss here the optimization of nanomagnets for spin qubits more specifically, these findings could be used in other domains where strong, nanoscale magnetic field gradients are desirable, e.g., in spintronics, in topological superconductivity [19–22], for magnetic actuation of nanoelements and nanobeads, or for scanning probe near-field magnetic sensing [23].

*william.legrand@mat.ethz.ch

†These two authors contributed equally.

In an initial step, we identify the ideal magnetization distributions that maximize a field or a gradient of any component, when no constraints are imposed on the magnetization. Even though these ideal-field distributions are not achievable in devices, they will allow us to deduce the best nanomagnet shapes when the geometrical constraints of nanofabrication are to be taken into account. These shapes can be adapted, for instance, to the cases of a double quantum dot defined in a two-dimensional electron gas or along a nanowire. We then consider systems of nanomagnets that are uniformly magnetized under an external field, as well as nanomagnets hosting magnetic domain walls, and compare the achieved field inhomogeneity for all combinations of three orthogonal orientations of magnetization and generated gradient.

The choice of the magnetic material composing the nanomagnets, which could differ from the commonly used elemental Co, is another aspect to consider. While a larger saturation magnetization generates stronger field gradients in the saturated case, it might not be true anymore when the internal dipolar interactions lead to the formation of inhomogeneous magnetic domains. We perform micromagnetic simulations to assess the requirements for keeping a uniform magnetization inside the nanomagnets, and thus for ensuring that they efficiently produce the desired field gradients. This provides, for a given saturation magnetization, a minimal value required for the external field, the resulting field gradients, and therefore a figure of merit for the achieved field inhomogeneity. We notably show that inhomogeneous components of the stray fields larger than their homogeneous components can be achieved, and predict a field difference of up to 500 mT between sites for CoFe nanomagnets and nanowire dots separated by up to 400 nm.

II. IDEAL-FIELD GRADIENT SOURCES

Along the following, we note $\mathbf{B}(\mathbf{r})$ the three-dimensional stray fields obtained from an ensemble of nanomagnets. Depending on the specific requirements of the system, it might be desired to optimize, for example, the absolute value of one component of the magnetic field or its inhomogeneity over some region(s) of interest. We write Q for this value to optimize, typically a single component of $\mathbf{B}(\mathbf{r})$ or one of its derivatives. The stray fields and their partial derivatives can be deduced from the distribution of elementary magnetic dipoles that fills the source nanomagnets, expressed by a volumic magnetization $\mathbf{M}(\mathbf{r}) = M_S\mathbf{m}(\mathbf{r})$, where M_S is the saturation magnetization of the magnetic material and $\mathbf{m}(\mathbf{r})$ is the unit vector giving the local orientation of the magnetization. The optimization of Q can be conveniently performed relying on the additivity of the magnetic stray fields with respect to the source magnetization distribution.

For each point of space, the best orientation of the local elementary dipole maximizing Q can be found. As long as there is only one linear quantity to optimize (as opposed to a ratio of them, for example), the problem remains linear and the optimal distribution of the magnetization together with the achieved field can be directly reconstructed. This approach is, in particular, also valid for the optimization of a field or a gradient difference between two regions, which is the main focus of this work.

We show several examples of optimal distributions of $\mathbf{m}(\mathbf{r})$ in Fig. 1. These differ by their polar profiles around $\mathbf{r} = 0$ where Q is evaluated, which originate from the form and symmetry of the dipole fields. Into details, we consider an elementary dipole located at $\mathbf{r}_j$ and a quantity Q to optimize at $\mathbf{r}_i$, their distance $r_{ji} = \left|\mathbf{r}_i - \mathbf{r}_j\right|$ and the orientation vector $\mathbf{e}_{ji} = (\mathbf{r}_i - \mathbf{r}_j)/r_{ji}$ (see Appendix A for a schematic description of coordinates), as well as $d\mu = M_S d^3 r_j$ the magnetic moment contained in the elementary volume at $\mathbf{r}_j$. Any field component, or its longitudinal and transverse gradients along an arbitrary direction, can be expressed after a choice of matching u, v, w Cartesian coordinates, for which we express only a minimal set of equations. We start from

$$d\mathbf{B}_{ji}\cdot\hat{\mathbf{u}} = \frac{\mu_0 d\mu}{4\pi r_{ji}^3}\left[3(\mathbf{e}_{ji}\cdot\hat{\mathbf{u}})(\mathbf{e}_{ji}\cdot\mathbf{m}_j) - \mathbf{m}_j\cdot\hat{\mathbf{u}}\right], \tag{1}$$

$$d\frac{\partial\mathbf{B}_{ji}\cdot\hat{\mathbf{u}}}{\partial u} = \frac{\mu_0 d\mu}{4\pi}\frac{\partial r_{ji}^{-3}}{\partial u}\left[3(\mathbf{e}_{ji}\cdot\hat{\mathbf{u}})(\mathbf{e}_{ji}\cdot\mathbf{m}_j) - \mathbf{m}_j\cdot\hat{\mathbf{u}}\right] + \frac{\mu_0 d\mu}{4\pi r_{ji}^3}\left[3\frac{\partial}{\partial u}(\mathbf{e}_{ji}\cdot\hat{\mathbf{u}})(\mathbf{e}_{ji}\cdot\mathbf{m}_j)\right], \tag{2}$$

$$d\frac{\partial\mathbf{B}_{ji}\cdot\hat{\mathbf{v}}}{\partial u} = \frac{\mu_0 d\mu}{4\pi}\frac{\partial r_{ji}^{-3}}{\partial u}\left[3(\mathbf{e}_{ji}\cdot\hat{\mathbf{v}})(\mathbf{e}_{ji}\cdot\mathbf{m}_j) - \mathbf{m}_j\cdot\hat{\mathbf{v}}\right] + \frac{\mu_0 d\mu}{4\pi r_{ji}^3}\left[3\frac{\partial}{\partial u}(\mathbf{e}_{ji}\cdot\hat{\mathbf{v}})(\mathbf{e}_{ji}\cdot\mathbf{m}_j)\right], \tag{3}$$

where $d\mathbf{B}_{ji}$ is the field generated at $\mathbf{r}_i$ by the elementary moment $d\mu$ at $\mathbf{r}_j$. Equations (1)–(3) describe a field, a longitudinal-field gradient and a transverse-field gradient optimization, respectively. It appears from Eqs. (1) and (2) that to maximize a field or longitudinal gradient, the local vector $\mathbf{m}_j$ at each $\mathbf{r}_j$ needs to be contained within the plane defined by $\mathbf{e}_{ji}$ and $\hat{\mathbf{u}}$. Indeed, for a given quantity dQ obtained with any $\mathbf{m}_j$ within this plane, letting a component of $\mathbf{m}_j$ transverse to this plane reduces all terms by a common factor. This property is also easily checked numerically. For Eq. (3) and a transverse gradient, the situation is more complex and leads to $\mathbf{m}_j$ not contained in this plane in the general case. For the simpler case of Fig. 1, however, $\mathbf{m}_j$ is still contained in the (u, v) plane. Hence, the formulas below apply to any plane for a field or longitudinal gradient and, for simplicity, are restrained to the

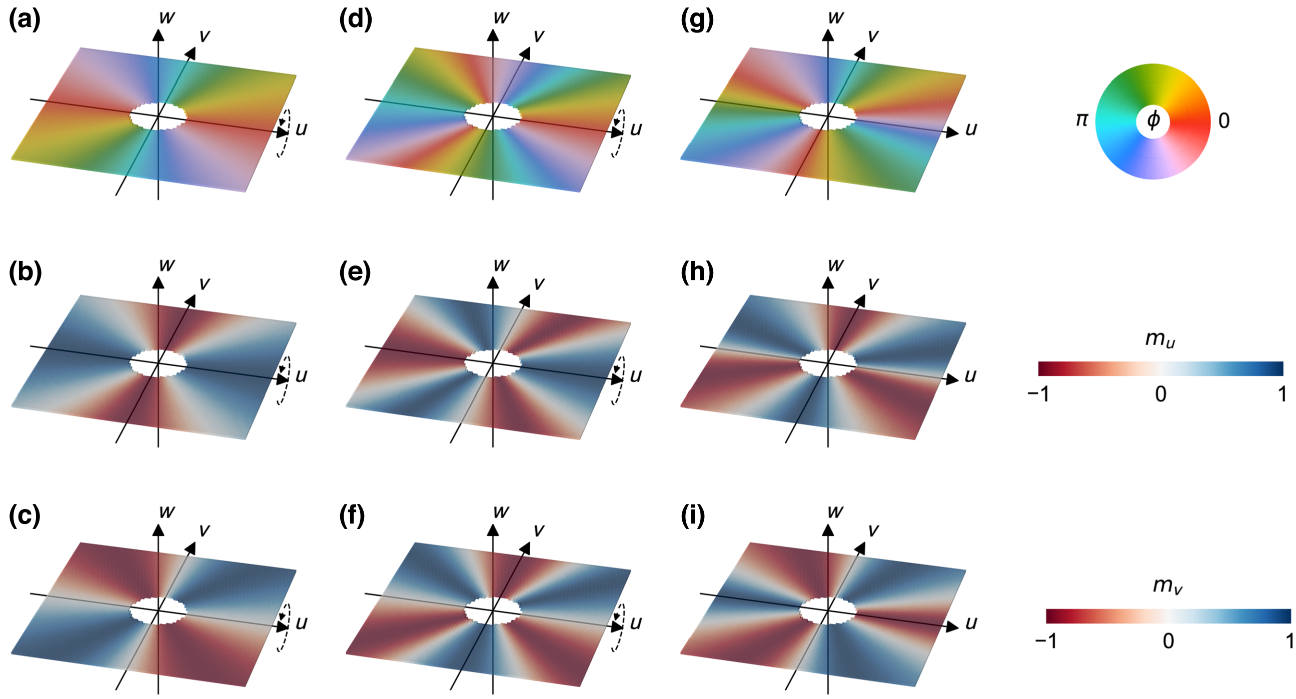

FIG. 1. Cut views in the (u, v) plane of the ideal magnetic distributions for optimizing (a)–(c) $B_u(0)$, (d)–(f) $\partial B_u/\partial u(0)$, and (g)–(i) $\partial B_v/\partial u(0)$. (a),(d),(g) show the in-plane angle ϕ, (b),(e),(h) show m_u, (c),(f),(i) show m_v for these optimal distributions, while m_w is zero within this plane for these three cases. Axes arrows for u, v, and w have the same relative length.

(u, v) plane for a transverse gradient. Writing ϕ for the in-plane angle between $\hat{\mathbf{u}}$ and $\mathbf{m}_j$ and θ for the in-plane angle between $\hat{\mathbf{u}}$ and $\mathbf{e}_{ji}$, we obtain that

$$d\mathbf{B}_{ji} \cdot \hat{\mathbf{u}} = \frac{\mu_0 d\mu}{4\pi r_{ji}^3} \left[3\cos\theta\cos(\phi - \theta) - \cos\phi\right], \tag{4}$$

$$d\frac{\partial \mathbf{B}_{ji} \cdot \hat{\mathbf{u}}}{\partial u} = -\frac{3\mu_0 d\mu}{4\pi r_{ji}^4} \left[\cos(\phi - 3\theta) + \cos^2\theta\cos(\phi - \theta)\right], \tag{5}$$

$$d\frac{\partial \mathbf{B}_{ji} \cdot \hat{\mathbf{v}}}{\partial u} = -\frac{3\mu_0 d\mu}{4\pi r_{ji}^4} \left[-\sin(\phi - 3\theta) + \cos\theta\sin\theta\cos(\phi - \theta)\right]. \tag{6}$$

Note that θ refers here to the polar angle of $\mathbf{r}_i$ defined with respect to $\mathbf{r}_j$. By defining $\theta' = \pi + \theta$, equivalent formulas as a function of $\mathbf{r}_j$ with respect to $\mathbf{r}_i$ can be obtained. To maximize $dQ = d\mathbf{B}_{ji} \cdot \hat{\mathbf{u}}$, $dQ = d\partial\mathbf{B}_{ji} \cdot \hat{\mathbf{u}}/\partial u$ or $dQ = d\partial\mathbf{B}_{ji} \cdot \hat{\mathbf{v}}/\partial u$ we find

$$\phi = \arctan\frac{3\sin 2\theta}{3\cos 2\theta + 1}, \tag{7}$$

$$\phi = \arctan\frac{-5\sin 3\theta - \sin\theta}{-5\cos 3\theta - 3\cos\theta}, \tag{8}$$

$$\phi = \arctan\frac{5\cos 3\theta - \cos\theta}{-5\sin 3\theta - \sin\theta}, \tag{9}$$

respectively, which are shown in Fig. 1. Here, arctan implies that the quadrant of the angle is chosen by the signs of the numerator and denominator.

This treatment resembles, but is not equivalent, to the original realization of multipole magnetic fields using permanent magnets by Halbach [24]. It is well known, for example, that the component of the field along the dipole direction is positive only within a cone originating from the dipole position, generated around the dipole axis with an angle of $\arccos(1/\sqrt{3}) \approx 54.7^\circ$. This is contained in the denominator of Eq. (7). In addition, Eqs. (7)–(9) explain why the optimal distributions for maximizing a component and a gradient of the stray fields see $\mathbf{m}_j$ rotating, respectively, 2 and 3 times when looping around the origin at $\mathbf{r}_i$ [24]. For more complex quantities Q that do not add up, a similar approach is possible but would require a nonlinear optimization [21,25].

These calculations reveal the ideal internal magnetization distributions that nanomagnets should tend to reproduce to optimize the stray fields and gradients they create. The full, three-dimensional optimal distributions are deduced from Fig. 1 by rotation of the figure plane around the u axis for the field and longitudinal gradient cases. However, this rotation symmetry is absent for the transverse gradient case (see the full representations of this distribution in Appendix B). From these ideal distributions, it is possible to get an intuition of what would constitute the best magnet shapes, as we demonstrate below.

Beyond the shape of the nanomagnets, one other key aspect for field strength optimization is the minimal nanomagnet-to-dot distance. This appears clearly by considering an exclusion zone around the dot, of radius r, inside which no magnet can be present. This allows for taking into account several kinds of nanofabrication constraints preventing from reaching infinitely small sizes or strongly overlapping features. By performing the integration of $dQ = d\partial \mathbf{B}_{ji} \cdot \hat{\mathbf{u}}/\partial u$ ($dQ = d\partial \mathbf{B}_{ji} \cdot \hat{\mathbf{v}}/\partial u$) over the remaining space $r_{ji} > r$, we find that $Q \approx 3.353\, \mu_0 M_S/r$ ($Q \approx 2.832\, \mu_0 M_S/r$). For $dQ = d\mathbf{B}_{ji} \cdot \hat{\mathbf{u}}$, we have to introduce also a maximum radius R, in which case we find $Q \approx 1.380\, \mu_0 M_S \ln(R/r)$. This sets a fundamental upper limit on the achievable gradients, and shows that for creating a large field difference between the dots, the nanomagnets need to extend as close as possible from the dots.

III. REALIZATION WITH SATURATED NANOMAGNETS AND DOMAIN WALLS

To progress further in the description of realistic magnetic field gradient sources, it is required to be more specific on the quantity to optimize. We let aside the generation of a localized gradient in a single dot [26] and focus on the generation of a field difference between two dots in a double quantum dot (DQD) system [3,9,11,14,27–30], as a similar approach works in both cases. An electron in the DQD system is confined to within a local area or length by an electrostatic potential. Considering dots placed symmetrically with respect to the field distribution, the fields in the two dots of the DQD will be composed of both a symmetric and an antisymmetric part. We may define, for each field component $i = u, v, w$,

$$B_i^{\mathrm{S,AS}} = (B_i^R \pm B_i^L)/2, \tag{10}$$

where $p = L, R$ stand for the left and right dot locations. The effects of the stray fields on the energies in the left and right part of the DQD can then be expressed by (see Appendix C)

$$\alpha_{\mathrm{S,AS}} = 2\mu_B \int \sqrt{\sum_i \left(B_i^{\mathrm{S,AS}}(\mathbf{r})\right)^2} \left|\psi_p(\mathbf{r})\right|^2 d\mathbf{r}, \tag{11}$$

where $\left|\psi_p(\mathbf{r})\right|^2$ is the probability of the presence of the electron in dot p, the prefactor 2 stands for the Landé factor of the electron spin and μ_B is the Bohr magneton. This supposes a spin quantization axis along B^{S} or B^{AS} and to neglect the dots overlap. Due to the nanomagnet symmetries in some optimized cases, one of the three components of $B_i^{\mathrm{S,AS}}$ is possibly zero; otherwise, the different field components containing a symmetric or an antisymmetric part are combined into α_{S} and α_{AS}. This corresponds to finding the symmetric and antisymmetric field quantization axes for the two dots. The gradient should thus be seen as an inhomogeneity between two sites of the fields averaged over each dot. This extension modifies the optimal distributions shown above, due to their convolution with the probability of presence functions $\left|\psi_p(\mathbf{r})\right|^2$. For simplicity, in Sec. III A we first introduce the general concept by considering two punctual sites as ideal dots. We present later, in Sec. III C, the effects of the average described above in the optimization of $\alpha_{\mathrm{S,AS}}$.

Most of the time, it will not be possible to impose the distribution of dipoles within the nanomagnets as finely as in Fig. 1, for two main reasons: the need for an external magnetic field to be applied to the devices, and the disturbance from internal dipolar interactions. Both will favor magnetic configurations inside the nanomagnets that are different from the ideal ones for field and gradient generation. It is also necessary to consider the constraint of a planar film geometry, due to available deposition techniques and integration of the nanomagnets in the device layout. We may consider an in-plane magnetization (due to the shape anisotropy of planar films, added to the requirement of employing in-plane external magnetic fields to ensure compatibility with standard superconducting microwave resonators). Another avenue is to use magnetic materials with strong out-of-plane magnetic anisotropy that do not require out-of-plane external magnetic fields during operation.

With these constraints in mind, a relevant design approach to maximize the field difference between the two dots is to consider uniformly magnetized nanomagnets restrained to a finite thickness. Their uniform magnetization can be easily ensured by saturation under a large external magnetic field in the in-plane case, or a large magnetic anisotropy in the out-of-plane case, which are both able to overcome internal magnetostatic fields. In this approach, the optimization simply consists in deciding at each point of space whether part of a magnet should be placed there. This choice naturally depends on whether the corresponding elementary dipole increases Q, given its externally imposed magnetization $\mathbf{m}$. In turn, this determines the optimal shapes for saturated nanomagnets.

A. Punctual dots

We first consider ideally punctual dots, such that $\left|\psi_p(\mathbf{r})\right|^2$ is nonzero only at the two points L and R and thus, the value to optimize is simply $Q = B_i^R - B_i^L$. The shapes generating the strongest field differences within such an ideal DQD system are shown in Figs. 2(a)–2(i), for the u, v, w magnetic orientations and a difference of B_u, B_v, B_w fields. This example consists of a typical DQD system where the dots are separated by 100 nm and buried 100 nm below the magnetic layer of thickness 200 nm across w. Results for other values of these parameters are provided in Appendix D. The shapes appearing in Figs. 2(a)–2(i)

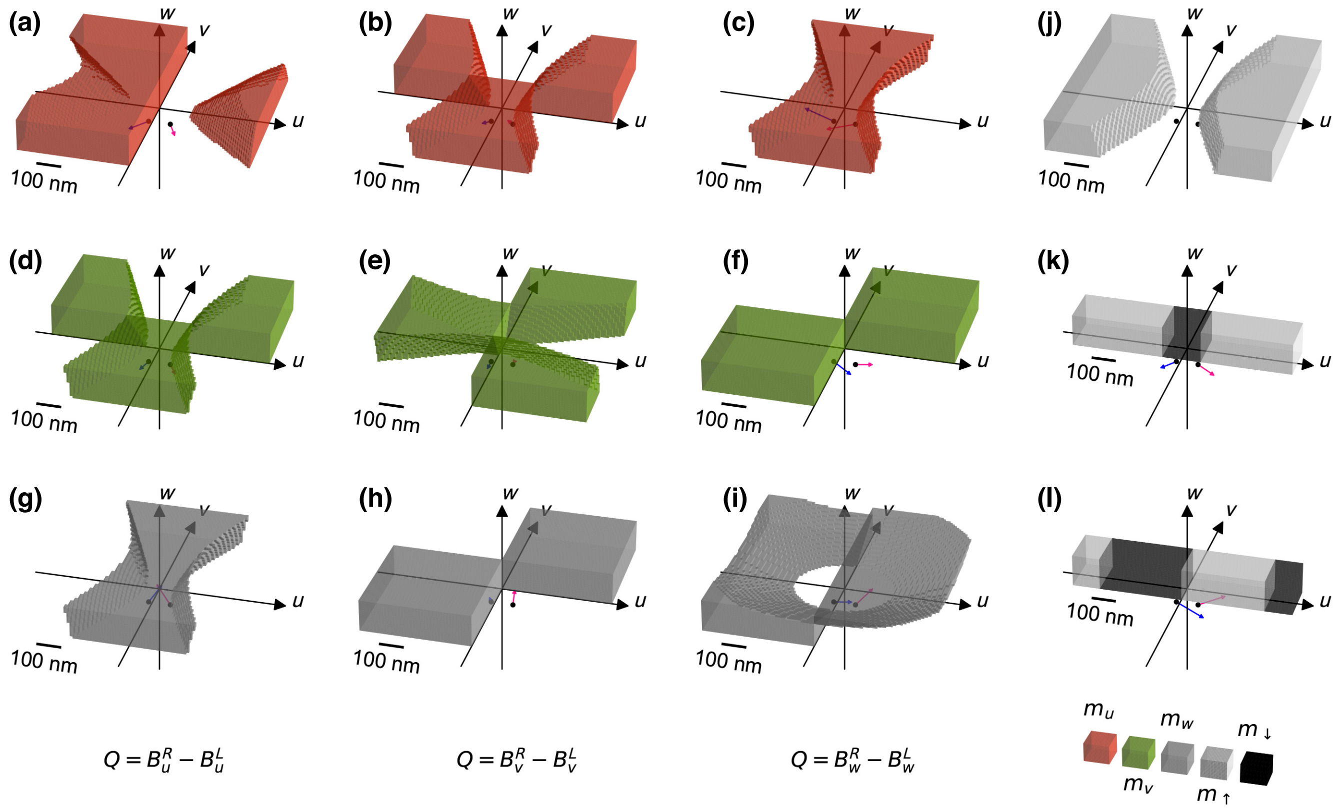

FIG. 2. (a)–(j) Three-dimensional views of optimal, uniformly magnetized nanomagnets generating a field difference in a double quantum dot system. Uniform magnetization imposed along (a)–(c) u, (d)–(f) v, and (g)–(i) w directions maximizing field difference for (a),(d),(g) B_u, (b),(e),(h) B_v, and (c),(f),(i) B_w. (j) Complementary shape to cases (c) and (g), maximizing a positive field difference of B_u and B_w. (k),(l) Domain-wall nanomagnets maximizing field difference for (k) B_u and (l) B_w. The light (dark) color filling corresponds to $\mathbf{m}$ along w ($-w$). Dot locations are indicated by the pair of points, and fields in the left and right dots by blue and magenta arrows, respectively, with scale 1 μm $/\mu_0 M_S$. Axes arrows for u, v, and w have the same length, scale bar equals both the interdot distance and dot depth of 100 nm.

are explained by the predictions of the ideal case presented above. Considering the ideal magnetic distributions $\mathbf{m}^{\text{opt}}$ from Figs. 1(e), 1(f), 1(h), 1(i), the suitable shape for a uniformly magnetized magnet with $m_{u,v,w} = 1$ can be qualitatively found, with satisfying accuracy, by taking the region of space for which $\mathbf{u}, \mathbf{v}, \mathbf{w} \cdot \mathbf{m}^{\text{opt}} > 0$.

In two cases, for a uniform magnetization along $\mathbf{u}$ generating a B_w field difference [Fig. 2(c)] and for a uniform magnetization along $\mathbf{w}$ generating a B_u field difference [Fig. 2(g)], the nanomagnets have a particular symmetry. Their complementary shape, represented in Fig. 2(j), does not generate an equal field difference with opposite sign, but a lower difference instead. This is due to the finite thickness across w of the nanomagnets and their location above the dots.

It appears overall that two of these shapes are not easily realizable with common deposition and lithography techniques [Figs. 2(a), 2(i)], due to the requirement of having elevated portions compared to the reference plane $w = 0$. Note that considering three-dimensional shapes of nanofabricated magnets, as can be envisioned from recent promising results in the field [31], would allow to go beyond this restriction. Nevertheless, all the other configurations [Figs. 2(b)–2(h) and 2(j)] are close to a simple shape that can be obtained from a single and uniformly thick layer, avoiding the use of different thicknesses within one design. This set of simple configurations covers the needs for generating an asymmetric field component along the three possible directions u, v, w relative to the DQD axis.

The values of the symmetric and antisymmetric field components, obtained for the specific dimensions considered in the present example, are summarized in Table I. The space discretization has been set to cells of 5 nm to reach the third digit precision in this estimation. To account fully for cases (c) and (g), we complete the table with the values obtained for their common complementary shape, case (j). It appears that in-plane transverse gradients [cases (d–f)] are more difficult to achieve, as revealed by their lower values for α_{AS}. Among the various results, the last case (j) of a longitudinal gradient produced with out-of-plane magnetization is noticeable. In comparison to all

TABLE I. Estimated field components in the DQD system for the configurations of Fig. 2.

Fig. 2 panel	**m** dir.	α_{AS} dir.	B_u^L	B_v^L	B_w^L ($\mu_0 M_S$)	B_u^R	B_v^R	B_w^R	$\alpha_{\mathrm{S}}/\mu_B$ ($\mu_0 M_S$)	$\alpha_{\mathrm{AS}}/\mu_B$
(a)	u	u	−0.097	0.000	−0.075	0.022	0.000	−0.081	0.174	0.119
(b)	u	v	−0.037	−0.035	0.003	−0.037	0.035	−0.003	0.075	0.071
(c)	u	w	−0.137	0.000	0.064	−0.137	0.000	−0.064	0.274	0.129
(d)	v	u	−0.035	−0.037	−0.038	0.035	−0.037	−0.038	0.106	0.070
(e)	v	v	−0.000	−0.073	−0.000	0.000	−0.001	0.000	0.074	0.072
(f)	v	w	0.092	−0.037	−0.047	0.092	−0.037	0.047	0.198	0.094
(g)	w	u	0.064	−0.000	0.133	−0.064	−0.000	0.133	0.266	0.129
(h)	w	v	0.003	−0.047	0.074	−0.003	0.047	0.074	0.149	0.094
(i)	w	w	0.088	−0.000	0.016	0.082	−0.000	0.132	0.226	0.116
(j)	u	w	0.062	0.000	−0.058	0.062	0.000	0.058	0.124	0.116
(j)	w	u	−0.058	0.000	0.016	0.058	−0.000	0.016	0.032	0.116
(k)	$w,-w$	u	−0.078	0.000	−0.058	0.078	0.000	−0.058	0.116	0.156
(l)	$w,-w$	w	0.128	0.000	−0.088	0.128	−0.000	0.088	0.256	0.176

other configurations, it allows for a much larger asymmetric component relative to the symmetric one, which therefore creates the most inhomogeneous field distribution. Two patterns among the ones shown in Fig. 2 are expected to be easier to implement in practice, cases (j) of a transverse gradient and (d). This is because the shape anisotropy from the different parts of the magnetic system favors the intended uniform magnetization, as will be shown later.

B. Nanomagnets with domain walls

An additional feature of nanomagnets is the possibility to host a magnetic domain wall. By allowing for opposite magnetization directions inside different domains, a larger portion of space can be filled with magnetic material, producing in turn a stronger gradient. Sharp and well-defined domain walls are easier to obtain in perpendicularly magnetized systems, as in magnetic multilayers with interfacial anisotropy, for example. By introducing a domain wall inside a perpendicularly magnetized nanomagnet, and provided the wall width is narrow compared to the other dimensions in the system, the magnetic system gets closer to an ideal gradient source. We still consider here punctual dots and $Q = B_i^R - B_i^L$. We present in Figs. 2(k), 2(l) the optimized nanomagnets with perpendicular magnetization and domain wall(s), now considering a nanomagnet width of 200 nm as well. A constraint was added that the domain wall is straight and contained within a plane perpendicular to u, which is the configuration observed in practice as it minimizes the domain-wall energy. Thus, this optimization consists in choosing a positive or negative $\mathbf{m} \cdot \mathbf{w}$ for all positions along u. A domain-wall pair is obtained for the case of a B_u field difference [Fig. 2(k)], while three domain walls (a single domain wall would suffice in a shorter nanomagnet) are obtained in the case of a B_w field difference [Fig. 2(l)]. The corresponding field values are reported in Table I as well. They confirm that a larger field difference is obtained, despite the smaller width of the nanomagnets.

C. Dots with finite extension

We now address in more detail the impact of the spatial extension of the individual dots of the DQD system. A pair of dots with linear confinement is now considered, as found in a nanowire DQD [32,33]. The dots are aligned along x and defined between −250 and −150 nm for dot L, and between 150 and 250 nm for dot R. The nanowire is suspended at $z = 200$ nm, above a magnetic layer extending across $-100 \text{ nm} < z < 100$ nm. Because the external magnetic field is preferably applied along the nanowire, while a transverse gradient is required, we rely on a uniform magnetization $\mathbf{m}$ along $+x$, and (u, v, w) matches with (x, y, z). As we now consider dots located above the magnetic system, we use $Q = \int B_{y,z}(x)\,|\psi_L(x)|^2\,dx - \int B_{y,z}(x)\,|\psi_R(x)|^2\,dx$ to optimize $\alpha_{\mathrm{S,AS}}$, where L and R are exchanged, compared to the above. To ensure practical shapes, a constraint was added that the magnet is homogeneous across z. Thus, this optimization consists in deciding the presence or absence of magnet in cells of the full thickness at all positions along x, y.

The resulting optimal nanomagnets for B_y and B_z difference are shown in Figs. 3(a)–3(d) and 3(e)–3(h), respectively. Similar to before, the shapes are explained by the ideal distributions, but are now convolved with the finite extension of the dots. The negligible differences in the present example are highlighted by Figs. 3(a), 3(e), which display the corresponding magnet boundaries with and without the finite size of dots for either B_y or B_z. This shows that in standard cases, the finite extension of the dots can be safely neglected in what concerns the design of the nanomagnets. The linear profiles of $\mathbf{B}(x)$ obtained along the nanowire are displayed in Figs. 3(c), 3(g). The relevant part of these profiles, determining the energy levels in the dots, is the one overlapping with $\left|\psi_p(\mathbf{r})\right|^2$ from each dot.

A relevant question beyond the shape of the nanomagnets is their expected footprint on a chip. It is thus desirable to know which parts of the nanomagnets are crucial to

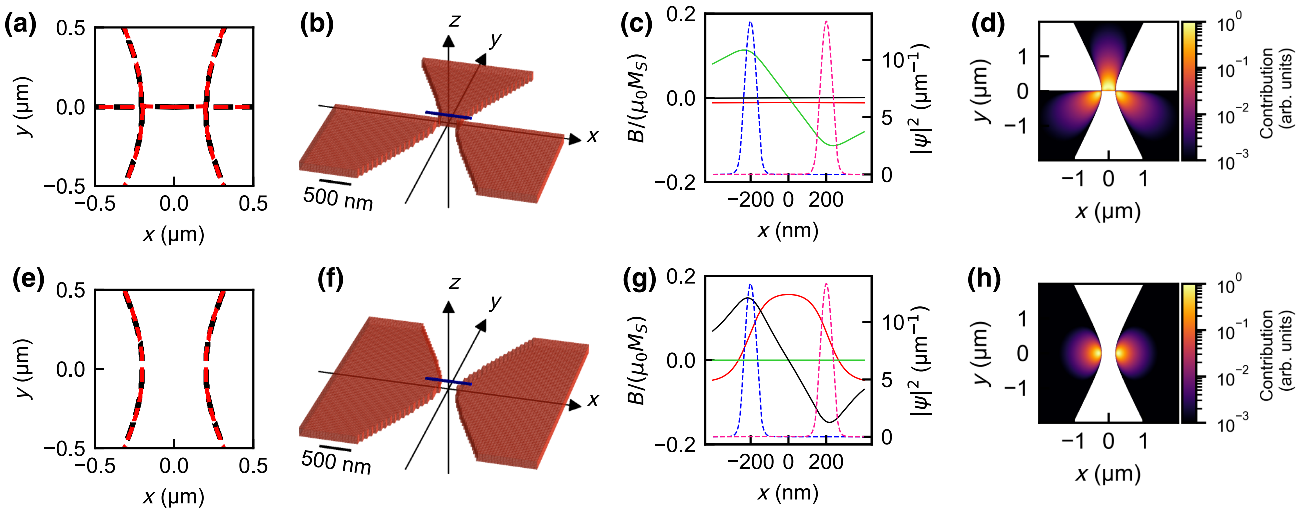

FIG. 3. Optimal shapes of a saturated nanomagnet in the case of dots of finite extension. Uniform magnetization imposed along x, maximizing (a)–(d) a B_y and (e)–(h) a B_z field difference. (a),(e) Limits of the optimized nanomagnets for two punctual dots (red lines) or two dots with spatial extension (black lines), and identical locations. (b),(f) Three-dimensional views of the nanomagnets obtained for finite-size dots. The nanowire location is indicated by the dark blue line. (c),(g) Profile of the stray magnetic fields along the nanowire (B_x in red, B_y in green, and B_z in black) and overlap with the probability of presence $|\psi_p(\mathbf{r})|^2$ of an electron in the left or right dot (respectively, in blue or magenta). (d),(h) Relative contributions, normalized to 1 for the largest value, of each part of the nanomagnet to the maximized quantity Q.

generate the gradient, and which parts can be disregarded. The significance of the contributions from each part of the nanomagnets to Q are shown in Figs. 3(d), 3(h). It confirms that the regions contributing the most to Q (or α_{AS}) are strongly localized near the dots. This highlights how critical mastering the nanofabrication processes is to achieve well-defined geometrical shapes at these internal edges of the nanomagnets.

IV. ACCURATE MODELING WITH MICROMAGNETIC OPTIMIZATION

The stray fields exhibited above are only valid under the condition of magnetic saturation of the nanomagnets. Even though an external field is usually applied to orientate the magnetic system, the internal magnetic interactions tend to disfavor this uniform magnetization and may lead to the formation of inhomogeneous domains inside the structures. For our previously optimized designs, we thus aim to find what minimum external field is required to ensure magnetic saturation, and to understand by how much the stray field gradients are affected when this condition is not met.

Having found optimal shapes for different uniform configurations above, we now consider an accurate modeling of all the magnetostatic interactions that will shape the internal magnetization of the nanomagnets. Micromagnetic simulations are able to capture the differences between a uniform magnetization and a spatially varying magnetization, affected by finite-size effects and internal interactions (direct exchange and dipolar terms). To illustrate our approach, micromagnetic simulations are performed with the MuMax^3 software [34] for a magnet of case (j) of Fig. 2 above. The simulated magnetic system has dimensions of $7000 \times 1000 \times 200$ nm^3 and a cell size of $4 \times 4 \times 4$ nm^3, see Appendix E for more details. Following magnetic saturation with an external field of 1 T, the stable magnetic configurations [35] under different values of the external field B_{ext} are obtained by decreasing steps of 100 mT.

Considering the saturation magnetization M_S of the magnetic material is useful for the present micromagnetic modeling, as it sets the energy scale of the dipolar interactions, entering as a quadratic term into the domain formation energy. While a larger M_S directly favors larger stray fields and gradients, it also facilitates the formation of magnetic domains in the nanomagnets and thus requires a larger external field to reach saturation. This external field adds up as a term $\alpha_{\mathrm{ext}} = 2\mu_B B_{\mathrm{ext}}$ to α_{S} from the symmetric part of the stray fields in forming the dots' energy levels. Defining the inhomogeneity of the fields acting on the dots as $\alpha_{\mathrm{AS}}/(\alpha_{\mathrm{S}} + \alpha_{\mathrm{ext}})$, this figure-of-merit value reduces when a large external field is employed. To optimize the inhomogeneity, it is thus required to identify the pairs of M_S and B_{ext} values providing the strongest $\alpha_{\mathrm{AS}}/(\alpha_{\mathrm{S}} + \alpha_{\mathrm{ext}})$.

Standard materials for nanomagnet fabrication include FeCo, Co, or NiFe, with values of M_S around 2000, 1450, and 800 kA m^{-1} at < 4 K temperatures, respectively. These values of M_S can be further adjusted down by alloying the ferromagnet with a nonmagnetic element, in order to reach a precise M_S requirement [36]. We present

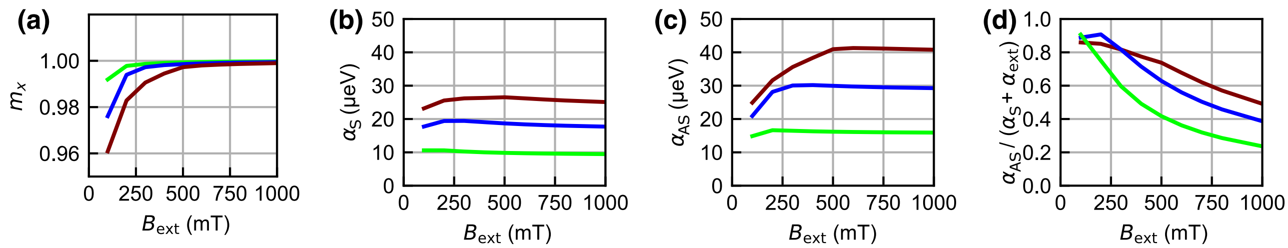

FIG. 4. Results of the micromagnetic simulations of an optimized shape for an inhomogeneous B_z component, with external field B_{ext} and magnetization along x. As a function of external magnetic field, (a) magnetization m_x, (b) symmetric (α_{S}), (c) antisymmetric (α_{AS}) coupling constants due to the nanomagnets, and (d) the ratio between the antisymmetric and the total symmetric field $\alpha_{\text{AS}}/(\alpha_{\text{S}} + \alpha_{\text{ext}})$. The different colors correspond to CoFe (red), Co (blue), and NiFe (green).

in Fig. 4(a) the evolution of the magnetization m_x, in Figs. 4(b), 4(c) that of the coupling terms α_{S} and α_{AS}, and in Fig. 4(d) that of the inhomogeneity ratio $\alpha_{\text{AS}}/(\alpha_{\text{S}} + \alpha_{\text{ext}})$, as a function of the external field and for these different M_S materials. It appears that within the usual range of employed external fields, the choice of magnetic material is a key parameter of the system, as saturation is reached at about 200 mT for NiFe, 300 mT for Co, and 600 mT for CoFe. To ensure reproducible fields at given conditions, it is necessary to ensure magnetic saturation. Depending on the admissible range of external fields in the system, and on whether a large inhomogeneity or a large nominal gradient of field is required, a particular pair of M_S and B_{ext} values might be more suitable. The example of Fig. 4(d), following the geometry of case (j) from Fig. 2, shows that the systems of nanomagnets presented here can reach a regime where $\alpha_{\text{AS}} \sim (\alpha_{\text{S}} + \alpha_{\text{ext}})$.

V. CONCLUSION

Despite its rather straightforward concepts, the present treatment provides a valuable and simple solution to the design of field gradients with nanomagnets. These are also compatible with rotated designs that allow for the differential tuning of the Zeeman energy splitting in different DQDs with tilted external fields [13], or with quantum dot arrays [37]. An extension of these ideas to the generation of cycloidal periodic fields, also of interest to shape synthetic spin-orbit coupling in quantum dots, nanowires, and two-dimensional electron gases [19–21,38], can, in principle, be realized by considering a periodic space for this optimization. The case of a perpendicularly magnetized system hosting domains has also been briefly presented. It may offer the opportunity of precisely controlling the position of the domain walls, or moving them continuously, in order to achieve reconfigurable magnetic field profiles in the nanomagnets, either with the help of notches [39] or of specific magnetic energy potential landscapes [40]. Such functionalities would need to be demonstrated in thick-patterned nanomagnets with perpendicular magnetic anisotropy. Taking into account also that a magnetic multilayer, such as Pt/Co or Co/Ni, provides the required out-of-plane anisotropy at the cost of a reduced M_S (due to the dilution of the magnetic moments inside a superstructure also containing less or nonmagnetic materials), it is left to future investigation to distinguish whether this can be beneficial overall.

The present approach is appealing for many material platforms hosting spin qubits: two-dimensional, such as silicon, germanium, graphene [41], or one-dimensional, such as semiconducting nanowires and carbon nanotubes [32,33], etc., as it does not rely on an intrinsic, defect-dependent spin-orbit interaction but on an extrinsic spin-orbit coupling tunable by the arrangement of nanomagnet shapes. For each of them, the achievable gradients are largely influenced by maximal interdot distance and minimal dot-to-nanomagnet separation. For nanowire spin qubits, this also provides an alternative to the use of ferromagnetic contacts [32,42].

These results will contribute to efforts for applying gate operations to distant spin qubits through their coupling to microwave radiation in high-impedance resonators at low powers (approximately single photon), in the framework of circuit quantum electrodynamics [41]. By comparing the benefits of strong spin-charge hybridization to decoherence contributions, it appears that a desirable regime for these operations is found around $\alpha_{\text{AS}} \sim \alpha_{\text{S}}$. This situation, where the strength of the antisymmetric component reaches the strength of the symmetric component of the stray fields, corresponds to a particularly high inhomogeneity. There, the effective fields acting over each dot point in directions differing by an angle of almost 90°. We find here some optimal shapes for nanomagnets that achieve this regime and that are feasible with standard nanofabrication techniques, enabling different field-gradient orientations. They offer an improvement of the magnetic field difference between dots by a factor at least 2 and up to 10, with respect to some earlier designs. As the energy associated to these fields determines the addressability of the spin qubits, improving the gradient will help moving beyond the perturbative regime of operation that has been commonly employed. With the results presented above, high-fidelity gate operations could be targeted in spin-qubit devices, while the optimized designs can also be applied to other research fields employing nanomagnets.

ACKNOWLEDGMENTS

We thank A. Thiaville for fruitful conversations and critical reading of the paper. We acknowledge funding from the PSPC-Regions No. 2 program awarded to the project "QUARBONE" (Grant No. 21006544), and from BPI France through its programs ADD, French Tech PIA1 - AGORANOV, and an i-LAB award "SCALE 12".

APPENDIX A: DEFINITION OF THE COORDINATE SYSTEM

In Fig. 5, the definitions for the coordinate system and the different angles relevant for the ideal distribution calculations are presented schematically, in the case of a B_u or a B_v field, or gradient.

APPENDIX B: ADDITIONAL REPRESENTATIONS FOR A TRANSVERSE GRADIENT IDEAL DISTRIBUTION

Figure 6 contains additional representations of the distribution of $\mathbf{m}$ for the lower-symmetry case of a transverse gradient generation with $dQ = d\partial\mathbf{B}_{ji} \cdot \hat{\mathbf{v}}/\partial u$. The plots display different planes offset from zero. The other cuts without offset, (u, w) and (v, w) planes, are not shown as they are either uniformly 0, or +1 and −1 either side of zero for m_u, m_v, and m_w.

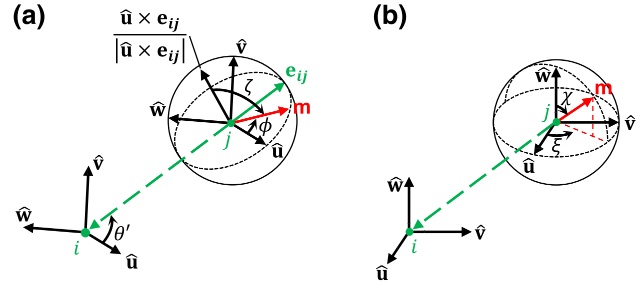

FIG. 5. Definition of coordinates system, with plane and angles considered. (a) Case of a B_u field or longitudinal gradient. All relevant angles θ' and ϕ are obtained in the plane defined by $\mathbf{u}$ and $\mathbf{e}_{ij}$. (b) General case, used for a transverse gradient, where no such plane reduction is possible.

APPENDIX C: DEFINITION OF THE MAGNETIC SYMMETRIC AND ANTISYMMETRIC COUPLINGS

A field B_L in the left dot and B_R in the right dot with equal modulus are assumed. As appears from Table I, this is the case for most geometries that we consider, at the exception of (a), (e), (i). In these cases, where fields have a different modulus, we can still define $\alpha_{\mathrm{S,AS}}$ to analyze the homogeneous and inhomogeneous parts of the fields in general, however, they are not sufficient to describe fully the DQD energies. For DQD spin operations, transverse-field gradients are required, i.e., all cases except (a), (e), (i). The two vectors B_L and B_R define a plane and θ_B is the angle between the two vectors, as depicted in Fig. 7. Then, a spin quantization axis at half the angle between the two magnetic field vectors B_L and B_R can always be chosen. By

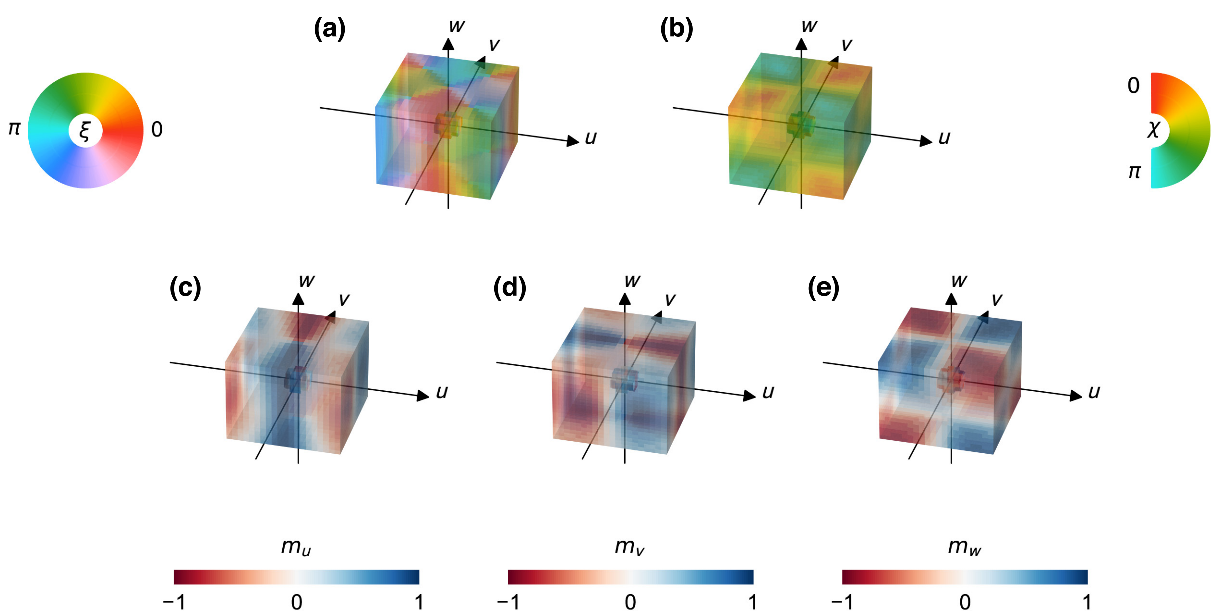

FIG. 6. Full views of the ideal magnetic distributions for optimizing $\partial B_v/\partial u(0)$: (a) in-plane angle ξ, (b) out-of-plane angle χ, (c) m_u, (d) m_v, and (e) m_w. Axes arrows for u, v, and w have the same relative length.

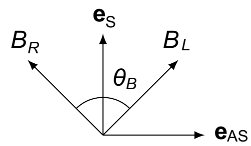

FIG. 7. Schematic representation of the spin quantization axes for the DQD, $\mathbf{e}_S$ and $\mathbf{e}_{AS}$, with respect to the left and right magnetic field in the DQD, B_L and B_R.

doing so, the component on $\mathbf{e}_S$ will be symmetric, while the component on the orthogonal vector $\mathbf{e}_{AS}$ will be antisymmetric. The potential associated to the magnetic field is $V_B = 2\mu_B \vec{B} \cdot \vec{\sigma}$, where $\vec{\sigma}$ is the Pauli vector. Finally, assuming that the wave functions are strongly localized in each dot leads to the potential

$$V_B = 2\mu_B \sum_p \int B_S(r)|\psi_p(r)|^2 dr\, \sigma_z + 2\mu_B \sum_p \tau_p \int B_{AS}(r)|\psi_p(r)|^2 dr\, \sigma_x, \qquad (C1)$$

where $p \in \{L, R\}$ and $\tau_p = 1 - 2\delta_{p,R}$. In Eq. (C1), B_S is defined as the projection of B_L and B_R on $\mathbf{e}_S$, and B_{AS} as the projection of B_L on $\mathbf{e}_{AS}$, which are, respectively, $(B_L + B_R)/2$ and $(B_L - B_R)/2$. Note that the use of σ_z as the spin operator for the symmetric axis is arbitrary.

APPENDIX D: ROLE OF MAGNET THICKNESS AND INTERDOT SPACING

The thickness of the magnetic layer and the spacing between the dots are fixed parameters in what is presented in the main text. In order to discuss the influence of these parameters on the α_{AS} term, we again consider a pair of nanowire quantum dots with linear confinement along the x axis, located 100 nm above a magnetic layer of finite thickness. Similar to the example of the main text, we optimize $Q = \int B_z(x)\,|\psi_L(x)|^2\,dx - \int B_z(x)\,|\psi_R(x)|^2\,dx$ to take into account the spatial extension of the dots.

The coupling constant α_{AS} can be computed for different values of the interdot separation distance and magnetic layer thickness. The results are presented in Figs. 8(a) and 8(b), respectively.

In Fig. 8(a), the interdot spacing is varied for a fixed thickness of the magnetic layer of 200 nm. Starting from low spacing values, increasing the distance between the dots increases the amplitude of the antisymmetric component field and thus of the coupling constant α_{AS}, because for a fixed magnet thickness, a similar gradient can be extended over a longer length, until reaching a limit value. This limit comes from the geometry: the field difference is limited by the maximum values of the field that can be reached, of order $\mu_0 M_S$ at most when the dots are not contained in the same layer than the magnetic patterns.

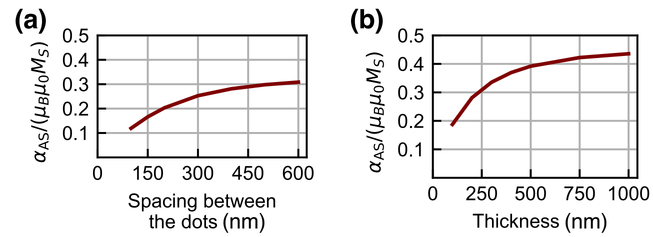

FIG. 8. Role of additional parameters in achieving a large field difference between the dots. (a) α_{AS} as a function of interdot spacing, fixed thickness of the magnetic layer of 200 nm. (b) α_{AS} as a function of thickness of the magnetic layer, fixed interdot spacing at 400 nm.

In practice, the spacing between the dots also cannot be increased excessively, as we want the dots to have some overlap, with a sufficient tunneling rate. For two dots confined in a nanowire, 400 nm remains a reasonable value for the spacing between the dots [33], which could enhance further their field difference. In Fig. 8(b), the thickness of the magnetic layer is varied for a fixed interdot spacing of 400 nm. Increasing the thickness of the magnetic layer improves α_{AS} until it reaches a maximum. Above a thickness of 500 nm, the evolution of α_{AS} and thus the amplitude of the antisymmetric component of the fields starts to saturate with the thickness of the magnetic layer. In the examples presented in the main text, a thickness of 200 nm is preferred as it simplifies the nanofabrication process and the integration of the double quantum dot in the designs.

APPENDIX E: MICROMAGNETIC SIMULATIONS

In order to obtain a uniform magnetization along any axis despite internal demagnetizing fields, it is advisable to induce a favorable shape anisotropy, while keeping unchanged the regions of the magnet contributing the most to α_{AS}. This allows in turn to reduce the minimal external field (here along x) required to saturate the magnet. Comparing between the optimized shapes of saturated nanomagnets, a shape anisotropy is easier to obtain with the geometry optimizing the field difference along the B_z component. We thus use this shape, keeping for MuMax^3 simulations a width (along y) of 1 μm and a length (along x) of 7 μm, which are the largest dimensions that could be simulated considering our hardware access. To avoid the effects of this finite length of the magnetic layer in

TABLE II. Magnetic parameters used in micromagnetic simulations.

Material	M_S (kA m^{-1})	A (pJ m^{-1})	Shape	Refs.
NiFe	800	13	Fig. 9	[43], [44]
Co	1450	56	Fig. 9	[45], [44]
CoFe	2000	20	Fig. 9	[46], [44]

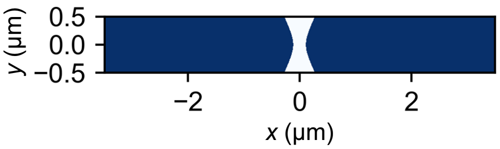

FIG. 9. Dimensions and geometry (blue color surface) of the simulated magnetic elements.

our simulations, while real magnets could be much longer, periodic boundary conditions are chosen in the x direction. The magnetic parameters considered for these simulations are listed in Table II.

The micromagnetic configurations at equilibrium are determined by reaching a configuration minimizing the total energy resulting from the exchange interaction between the spins, the internal dipolar interactions and the Zeeman energy. It is done for decreasing values of the external field, starting from magnetic saturation under a field of 1 T. We present in Fig. S1 within the Supplemental Material [35] two examples of minimal energy configurations that have been obtained. When saturation is lost, the reduction of the average m_x below 1 corresponds to the formation of closure domains at the extremities of the nanomagnets, affecting drastically the resulting gradient.

The stray fields at 100 nm above the surface of the magnetic layer can then be extracted from micromagnetic

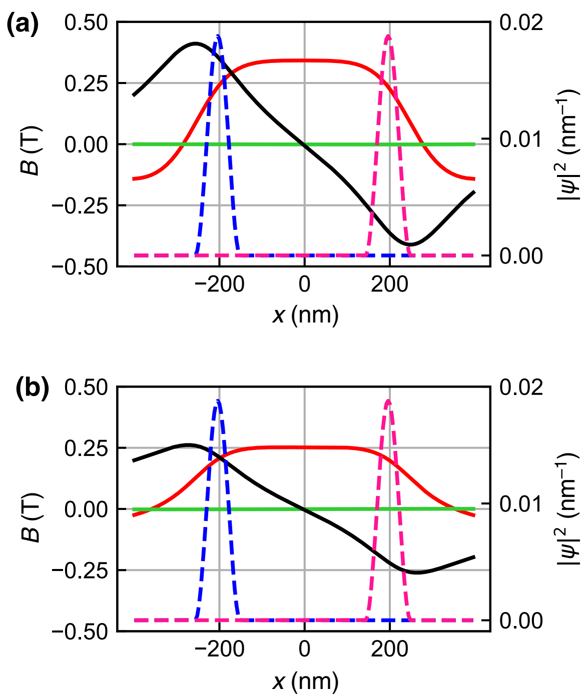

FIG. 10. Profile of the stray magnetic fields obtained from micromagnetic simulations in the case of CoFe nanomagnets, for (a) $B_{\text{ext}} = 500$ mT and (b) $B_{\text{ext}} = 100$ mT. B_x in red, B_y in green, and B_z in black, and overlap with the probability of the presence $|\psi_P(\mathbf{r})|^2$ of an electron in the left or right dot (respectively, in blue or magenta).

configurations as for the case of saturated magnets. The coupling constants α_{S} and α_{AS} are deduced from the linear profiles of the magnetic field $\mathbf{B}(x)$, as shown in Fig. 10.

[1] Y. Tokura, W. G. van der Wiel, T. Obata, and S. Tarucha, Coherent single electron spin control in a slanting Zeeman field, Phys. Rev. Lett. **96**, 047202 (2006).

[2] M. Pioro-Ladrière, T. Obata, Y. Tokura, Y.-S. Shin, T. Kubo, K. Yoshida, T. Taniyama, and S. Tarucha, Electrically driven single-electron spin resonance in a slanting Zeeman field, Nat. Phys. **4**, 776 (2008).

[3] T. Obata, M. Pioro-Ladrière, Y. Tokura, Y.-S. Shin, T. Kubo, K. Yoshida, T. Taniyama, and S. Tarucha, Coherent manipulation of individual electron spin in a double quantum dot integrated with a micromagnet, Phys. Rev. B **81**, 085317 (2010).

[4] X. Hu, Y. X. Liu, and F. Nori, Strong coupling of a spin qubit to a superconducting stripline cavity, Phys. Rev. B **86**, 035314 (2012).

[5] F. Beaudoin, D. Lachance-Quirion, W. A. Coish, and M. Pioro-Ladrière, Coupling a single electron spin to a microwave resonator: Controlling transverse and longitudinal couplings, Nanotechnology **27**, 464003 (2016).

[6] M. Benito, J. R. Petta, and G. Burkard, Optimized cavity-mediated dispersive two-qubit gates between spin qubits, Phys. Rev. B **100**, 081412(R) (2019).

[7] M. Pioro-Ladrière, Y. Tokura, T. Obata, T. Kubo, and S. Tarucha, Micromagnets for coherent control of spin-charge qubit in lateral quantum dots, Appl. Phys. Lett. **90**, 024105 (2007).

[8] D. Lachance-Quirion, J. C. Lemyre, L. Bergeron, C. Sarra-Bournet, and M. Pioro-Ladrière, Magnetometry of micromagnets with electrostatically defined Hall bars, Appl. Phys. Lett. **107**, 223103 (2015).

[9] X. Mi, M. Benito, S. Putz, D. M. Zajac, J. M. Taylor, G. Burkard, and J. R. Petta, A coherent spin–photon interface in silicon, Nature **555**, 599 (2018).

[10] N. I. Dumoulin Stuyck, F. A. Mohiyaddin, R. Li, M. Heyns, B. Govoreanu, and I. P. Radu, Low dephasing and robust micromagnet designs for silicon spin qubits, Appl. Phys. Lett. **119**, 094001 (2021).

[11] P. Harvey-Collard, J. Dijkema, G. Zheng, A. Sammak, G. Scappucci, and L. M. K. Vandersypen, Coherent spin-spin coupling mediated by virtual microwave photons, Phys. Rev. X **12**, 021026 (2022).

[12] J. Yoneda, K. Takeda, T. Otsuka, T. Nakajima, M. R. Delbecq, G. Allison, T. Honda, T. Kodera, S. Oda, Y. Hoshi, N. Usami, K. M. Itoh, and S. Tarucha, A quantum-dot spin qubit with coherence limited by charge noise and fidelity higher than 99.9%, Nat. Nanotechnol. **13**, 102 (2017).

[13] F. Borjans, X. G. Croot, X. Mi, M. J. Gullans, and J. R. Petta, Resonant microwave-mediated interactions between distant electron spins, Nature **577**, 195 (2019).

[14] K. Takeda, J. Kamioka, T. Otsuka, J. Yoneda, T. Nakajima, M. R. Delbecq, S. Amaha, G. Allison, T. Kodera, S. Oda, and S. Tarucha, A fault-tolerant addressable spin qubit in a natural silicon quantum dot, Sci. Adv. **2**, 1600694 (2016).

[15] R. P. G. McNeil, R. J. Schneble, M. Kataoka, C. J. B. Ford, T. Kasama, R. E. Dunin-Borkowski, J. M. Feinberg, R. J. Harrison, C. H. W. Barnes, D. H. Y. Tse, T. Trypiniotis, J. A. C. Bland, D. Anderson, G. A. C. Jones, and M. Pepper, Localized magnetic fields in arbitrary directions using patterned nanomagnets, Nano Lett. **10**, 1549 (2010).

[16] F. Forster, M. Mühlbacher, D. Schuh, W. Wegscheider, and S. Ludwig, Electric-dipole-induced spin resonance in a lateral double quantum dot incorporating two single-domain nanomagnets, Phys. Rev. B **91**, 195417 (2015).

[17] J. Yoneda, T. Otsuka, T. Takakura, M. Pioro-Ladrière, R. Brunner, H. Lu, T. Nakajima, T. Obata, A. Noiri, C. J. Palmstrøm, A. C. Gossard, and S. Tarucha, Robust micromagnet design for fast electrical manipulations of single spins in quantum dots, Appl. Phys. Express **8**, 084401 (2015).

[18] M. Aldeghi, R. Allenspach, and G. Salis, Modular nanomagnet design for spin qubits confined in a linear chain, Appl. Phys. Lett. **122**, 134003 (2023).

[19] T. Zhou, N. Mohanta, J. E. Han, A. Matos-Abiague, and I. Žutić, Tunable magnetic textures in spin valves: From spintronics to Majorana bound states, Phys. Rev. B **99**, 134505 (2019).

[20] V. Kornich, M. G. Vavilov, M. Friesen, M. A. Eriksson, and S. N. Coppersmith, Majorana bound states in nanowire-superconductor hybrid systems in periodic magnetic fields, Phys. Rev. B **101**, 125414 (2020).

[21] S. Turcotte, S. Boutin, J. C. Lemyre, I. Garate, and M. Pioro-Ladrière, Optimized micromagnet geometries for Majorana zero modes in low g-factor materials, Phys. Rev. B **102**, 125425 (2020).

[22] M. J. A. Jardine, J. P. T. Stenger, Y. Jiang, E. J. de Jong, W. Wang, A. C. B. Jayich, and S. M. Frolov, Integrating micromagnets and hybrid nanowires for topological quantum computing, SciPost Phys. **11**, 090 (2021).

[23] J. G. Longenecker, H. J. Mamin, A. W. Senko, L. Chen, C. T. Rettner, D. Rugar, and J. A. Marohn, High-gradient nanomagnets on cantilevers for sensitive detection of nuclear magnetic resonance, ACS Nano **6**, 9637 (2012).

[24] K. Halbach, Design of permanent multipole magnets with oriented rare earth cobalt material, Nucl. Instrum. Methods **169**, 1 (1980).

[25] C. Abert, C. Huber, F. Bruckner, C. Vogler, G. Wautischer, and D. Suess, A fast finite-difference algorithm for topology optimization of permanent magnets, J. Appl. Phys. **122**, 113904 (2017).

[26] E. Kawakami, P. Scarlino, D. R. Ward, F. R. Braakman, D. E. Savage, M. G. Lagally, M. Friesen, S. N. Coppersmith, M. A. Eriksson, and L. M. K. Vandersypen, Electrical control of a long-lived spin qubit in a Si/SiGe quantum dot, Nat. Nanotechnol. **9**, 666 (2014).

[27] E. A. Laird, C. Barthel, E. I. Rashba, C. M. Marcus, M. P. Hanson, and A. C. Gossard, Hyperfine-mediated gate-driven electron spin resonance, Phys. Rev. Lett. **99**, 246601 (2007).

[28] Y.-S. Shin, T. Obata, Y. Tokura, M. Pioro-Ladrière, R. Brunner, T. Kubo, K. Yoshida, and S. Tarucha, Single-spin readout in a double quantum dot including a micromagnet, Phys. Rev. Lett. **104**, 046802 (2010).

[29] J. Yoneda, T. Otsuka, T. Nakajima, T. Takakura, T. Obata, M. Pioro-Ladrière, H. Lu, C. J. Palmstrøm, A. C. Gossard, and S. Tarucha, Fast electrical control of single electron spins in quantum dots with vanishing influence from nuclear spins, Phys. Rev. Lett. **113**, 267601 (2014).

[30] N. Samkharadze, G. Zheng, N. Kalhor, D. Brousse, A. Sammak, U. C. Mendes, A. Blais, G. Scappucci, and L. M. K. Vandersypen, Strong spin-photon coupling in silicon, Science **359**, 1123 (2018).

[31] A. Fernández-Pacheco, R. Streubel, O. Fruchart, R. Hertel, P. Fischer, and R. P. Cowburn, Three-dimensional nanomagnetism, Nat. Commun. **8**, 15756 (2017).

[32] J. J. Viennot, M. C. Dartiailh, A. Cottet, and T. Kontos, Coherent coupling of a single spin to microwave cavity photons, Science **349**, 408 (2015).

[33] T. Cubaynes, M. R. Delbecq, M. C. Dartiailh, R. Assouly, M. M. Desjardins, L. C. Contamin, L. E. Bruhat, Z. Leghtas, F. Mallet, A. Cottet, and T. Kontos, Highly coherent spin states in carbon nanotubes coupled to cavity photons, Npj Quantum Inf. **5**, 47 (2019).

[34] A. Vansteenkiste, J. Leliaert, M. Dvornik, M. Helsen, F. Garcia-Sanchez, and B. Van Waeyenberge, The design and verification of MuMax3, AIP Adv. **4**, 107133 (2014).

[35] See Supplemental Material at http://link.aps.org/supplemental/10.1103/PhysRevApplied.20.044062 for representations of the magnetic configurations obtained from micromagnetic simulations.

[36] C. Eyrich, A. Zamani, W. Huttema, M. Arora, D. Harrison, F. Rashidi, D. Broun, B. Heinrich, O. Mryasov, M. Ahlberg, O. Karis, P. E. Jönsson, M. From, X. Zhu, and E. Girt, Effects of substitution on the exchange stiffness and magnetization of Co films, Phys. Rev. B **90**, 235408 (2014).

[37] S. Nakamura, H. Kiyama, and A. Oiwa, Micromagnet design for addressable fast spin manipulations in a 2×2 quantum dot array, J. Appl. Phys. **132**, 224301 (2022).

[38] N. Mohanta, T. Zhou, J.-W. Xu, J. E. Han, A. D. Kent, J. Shabani, I. Žutić, and A. Matos-Abiague, Electrical control of Majorana bound states using magnetic stripes, Phys. Rev. Appl. **12**, 034048 (2019).

[39] D. Petit, A.-V. Jausovec, D. Read, and R. P. Cowburn, Domain wall pinning and potential landscapes created by constrictions and protrusions in ferromagnetic nanowires, J. Appl. Phys. **103**, 114307 (2008).

[40] M. Negotia, M. P. P. Hodges, M. T. Bryan, P. W. Fry, M.-Y. Im, P. Fischer, D. A. Allwood, and T. J. Hayward, Linear transport of domain walls confined to propagating 1-D potential wells, J. Appl. Phys. **114**, 163901 (2013).

[41] G. Burkard, M. J. Gullans, X. Mi, and J. R. Petta, Superconductor–semiconductor hybrid-circuit quantum electrodynamics, Nat. Rev. Phys. **2**, 129 (2020).

[42] A. Cottet and T. Kontos, Spin quantum bit with ferromagnetic contacts for circuit QED, Phys. Rev. Lett. **105**, 160502 (2010).

[43] N. Sorensen, R. E. Camley, and Z. Celinski, Exchange stiffness as a function of composition in $Cu_x(Ni_{0.80}Fe_{0.20})_{1-x}$ alloys, J. Magn. Magn. Mater. **477**, 344 (2019).

[44] T. Thomson, in *Metallic Films for Electronic, Optical and Magnetic Applications* (Woodhead Publishing, Sawston, United Kingdom, 2014), p. 454.

[45] M. D. Kuz'Min, K. P. Skokov, L. V. B. Diop, I. A. Radulov, and O. Gutfleisch, Exchange stiffness of ferromagnets, Eur. Phys. J. Plus **135**, 301 (2020).

[46] H. S. Jung, W. D. Doyle, and S. Matsunuma, Influence of underlayers on the soft properties of high magnetization FeCo films, J. Appl. Phys. **93**, 6462 (2003).